

# On multicomponent polariton superfluidity in the optical parametric oscillator regime

A. C. Berceanu,<sup>1</sup> L. Dominici,<sup>2,3,\*</sup> I. Carusotto,<sup>4</sup> D. Ballarini,<sup>2,3</sup> E. Cancellieri,<sup>5</sup> G. Gigli,<sup>2</sup> M. H. Szymańska,<sup>6</sup> D. Sanvitto,<sup>2</sup> and F. M. Marchetti<sup>1,†</sup>

<sup>1</sup>*Departamento de Física Teórica de la Materia Condensada & Condensed Matter Physics Center (IFIMAC), Universidad Autónoma de Madrid, Madrid 28049, Spain*

<sup>2</sup>*NNL, Istituto Nanoscienze-CNR, Via Arnesano, 73100 Lecce, Italy*

<sup>3</sup>*Istituto Italiano di Tecnologia, IIT-Lecce, Via Barsanti, 73010 Lecce, Italy*

<sup>4</sup>*INO-CNR BEC Center and Università di Trento, via Sommarive 14, I-38123 Povo, Italy*

<sup>5</sup>*Department of Physics and Astronomy, University of Sheffield, Sheffield, S3 7RH, UK*

<sup>6</sup>*Department of Physics and Astronomy, University College London, Gower Street, London, WC1E 6BT, UK*

(Dated: March 12, 2015)

Superfluidity, the ability of a liquid or gas to flow with zero viscosity, is one of the most remarkable implications of collective quantum coherence. In equilibrium systems like liquid  $^4\text{He}$  and ultracold atomic gases, superfluid behaviour conjugates diverse yet related phenomena, such as persistency of metastable flow in multiply connected geometries and the existence of a critical velocity for frictionless flow when hitting a static defect. The link between these different aspects of superfluid behaviour is far less clear in driven-dissipative systems displaying collective coherence, such as microcavity polaritons, which raises important questions about their concurrency. With a joint theoretical and experimental study, we show that the scenario is particularly rich for polaritons driven in a three-fluid collective coherent regime so-called optical parametric oscillator. On the one hand, the spontaneous macroscopic coherence following the phase locking of the signal and idler fluids has been shown to be responsible for their simultaneous quantized flow metastability. On the other hand, we show here that pump, signal and idler have distinct responses when hitting a static defect; while the signal displays hardly appreciable modulations, the ones appearing in pump and idler are determined by their mutual coupling due to nonlinear and parametric processes.

PACS numbers: 03.75.Kk, 71.36.+c, 42.65.Yj

## I. INTRODUCTION

Microcavity polaritons, the novel quasiparticles resulting from the coherent strong coupling between quantum well excitons and cavity photons<sup>1</sup>, have unique mixed matter-light properties that none of their constituents displays on its own. Because of their energy dispersion and their strong non-linearity inherited from the excitonic components, polaritons continuously injected by an external laser into a pump state with suitable wavevector and energy can undergo coherent stimulated scattering into two conjugate states<sup>2-4</sup>, the signal and the idler, a process known as optical parametric oscillator (OPO). Since their first realisation<sup>5-9</sup>, the interest in microcavity optical parametric phenomena has involved several fields of fundamental and applicative research<sup>10-16</sup>.

Recently, considerable resources have been invested in exploring the fundamental properties of parametric processes, including the possibility of macroscopic phase coherence and superfluid behaviour<sup>17</sup>. In spite of the coherent nature of the driving laser pump, the OPO process belongs to the class of non-equilibrium phase transitions, in which a  $U(1)$  phase symmetry is spontaneously broken<sup>18</sup>. While the phase of the pumped mode is locked to the incident laser, the ones of signal and idler are free to be simultaneously rotated in opposite directions. Because of this phase freedom, recent experiments<sup>19</sup> have tested the OPO superfluid properties by exploring the physics of the signal-idler order parameter, demonstrat-

ing the existence and metastability of vortex configurations. As the order parameter involves both signal and idler, their phase winding have opposite signs<sup>19-21</sup>. Crucially, this makes both OPO fluids to display quantized flow metastability simultaneously.

While in equilibrium condensates different aspects of superfluidity are typically closely related<sup>22</sup>, this is no longer true in a non-equilibrium context as for microcavity polaritons<sup>17</sup>. In particular, those aspects of superfluidity related to the frictionless flow around defects are expected to be much more involved in OPO condensates than for any other investigated polariton condensates, such as for the case of incoherent pumping<sup>23,24</sup>, and single-state resonantly pumped microcavities<sup>25</sup>. Independently on the pumping scheme, the driving and the polariton finite lifetime prompt questions about the meaning of superfluid behaviour, when the spectrum of collective excitations is complex rather than real, raising conceptual interrogatives about the applicability of a Landau criterion<sup>24</sup>. Yet, an additional complexity characterises the OPO regime, where the simultaneous presence of three oscillation frequencies and momenta for pump, signal and idler correspondingly multiplies the number of collective excitation branches<sup>18</sup>. Note that from the experimental point of view, pioneering experiments<sup>26</sup> have observed a ballistic non-spreading propagation of signal/idler polariton wavepackets in a triggered-OPO configuration. However, given the complexity of the dynamics as well as the nonlinear interactions involved in this time-dependent configuration<sup>27</sup>, theoretical un-

derstanding of these observations is not complete yet.

This Article reports a joint theoretical and experimental study of an OPO configuration where a wide and steady-state condensate hits a stationary localised defect in the microcavity. Contrary to the criterion for quantized flow metastability for which signal and idler display simultaneous locked responses, we find that their scattering properties when the OPO hits a static defect are different. In particular we investigate the scattering properties of all three fluids, pump, signal and idler, in both real and momentum space. We find that the modulations generated by the defect in each fluid are determined not only by its associated Rayleigh scattering ring, but each component displays additional rings because of the cross-talk with the other components imposed by non-linear and parametric processes. We single out three factors determining which one of these rings influences the most each fluid response: the coupling strength between the three OPO states, the resonance of the ring with the blue-shifted lower polariton dispersion, the values of each fluid group velocity and lifetime together establishing how far each modulation can propagate from the defect. The concurrence of these effects implies that the idler strongly scatters inheriting the same modulations as the pump, while the modulations due to its own ring can propagate only very close to the defect and cannot be appreciated. Yet, the modulations in the signal are strongly suppressed, and not at all visible in experiments, because the slope of the polariton dispersion in its low momentum component brings all Rayleigh rings coming from pump and idler out of resonance.

Note that the kinematic conditions for OPO are incompatible with the pump and idler being in the subsonic regime. Thus, the coupling between the three components always implies some degree of scattering in the signal. In practice, the small value of the signal momentum strongly suppresses its actually visible modulations, something confirmed by the experimental observations.

## II. MODEL

The dynamics of polaritons in the OPO regime, and their hydrodynamic properties when scattering against a defect, can be described via a classical driven-dissipative non-linear Gross-Pitaevskii equation (GPE) for the coupled exciton and cavity fields  $\psi_{X,C}(\mathbf{r}, t)$  ( $\hbar = 1$ )<sup>17,28</sup>:

$$i\partial_t \begin{pmatrix} \psi_X \\ \psi_C \end{pmatrix} = \hat{H} \begin{pmatrix} \psi_X \\ \psi_C \end{pmatrix} + \begin{pmatrix} 0 \\ F_p(\mathbf{r}, t) \end{pmatrix}. \quad (1)$$

The dispersive  $X$ - and  $C$ -fields decay at a rate  $\gamma_{X,C}$  and are coupled by the Rabi splitting  $\Omega_R$ , while the non-linearity is regulated by the exciton coupling strength  $g_X$ :

$$\hat{H} = \begin{pmatrix} \omega_{-i\nabla}^X - i\frac{\gamma_X}{2} + g_X|\psi_X|^2 & \Omega_R/2 \\ \Omega_R/2 & \omega_{-i\nabla}^C - i\frac{\gamma_C}{2} + V_d \end{pmatrix}. \quad (2)$$

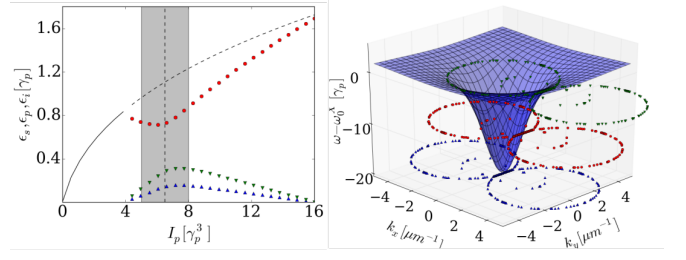


FIG. 1. (Color online) OPO mean-field blue-shifts and fluctuation Rayleigh rings in the linear response scheme for homogeneous pumping. Left panel: Signal  $s$  ([blue] upper triangles), pump  $p$  ([red] circles), and idler  $i$  ([green] lower triangles) mean-field energy blue-shifts  $\epsilon_{n=s,p,i}$  (in units of  $\gamma_p = \gamma_{\mathbf{k}_p}$ ) versus the rescaled pump intensity  $I_p$  (in units of  $\gamma_p^3$ ) in the optical limiter regime. Parameters are  $\Omega_R = 5$  meV, zero cavity-exciton detuning,  $\gamma_X = \gamma_C = 0.12$  meV,  $\omega_p - \omega_0^X = -1.25$  meV,  $k_p = 1.6\mu\text{m}^{-1}$ ,  $k_s \simeq 0$ , and  $k_i = 3.2\mu\text{m}^{-1}$ . The shaded area is stable OPO region, while the vertical dashed line corresponds to the pump power value chosen for plotting the right panel. Right panel: Blue-shifted LP dispersion (10) with superimposed Rayleigh curves  $\Gamma_{p,i,(u,v),\tilde{\mathbf{k}}+\mathbf{k}_{p,i}}$  evaluated within the linear response approximation (same symbols as left panel). The two rings corresponding to the signal state,  $\Gamma_{s,(u,v),\tilde{\mathbf{k}}}$ , are shrunk to zero because  $k_s \simeq 0$ .

We describe the defect via a potential  $V_d(\mathbf{r})$  acting on the photonic component; this can either be a defect in the cavity mirror or a localised laser field<sup>25,29,30</sup>. In the conservative, homogeneous, and linear regime ( $\gamma_{X,C} = 0 = V_d(\mathbf{r}) = g_X$ ), the eigenvalues of  $\hat{H}$  are given by the lower (LP) and upper polariton (UP) energies,  $2\omega_{\mathbf{k}}^{LP,UP} = \omega_{\mathbf{k}}^C + \omega_{\mathbf{k}}^X \mp \sqrt{(\omega_{\mathbf{k}}^C - \omega_{\mathbf{k}}^X)^2 + \Omega_R^2}$ . The cavity is driven by a continuous-wave laser field  $F_p(\mathbf{r}, t) = \mathcal{F}_p(\mathbf{r})e^{i(\mathbf{k}_p \cdot \mathbf{r} - \omega_p t)}$  into the OPO regime: Here, polaritons are continuously injected into the pump state with frequency  $\omega_p$  and momentum  $\mathbf{k}_p$  and, above a pump strength threshold, undergo coherent stimulated scattering into the signal ( $\omega_s, \mathbf{k}_s$ ) and idler ( $\omega_i, \mathbf{k}_i$ ) states.

As a first step, it is useful to get insight into the system behaviour in the simple case of a homogeneous pump of strength  $\mathcal{F}_p(\mathbf{r}) = f_p$ . A numerical study of the coupled equations (1) for the more realistic case of a finite-size top-hat pump profile  $\mathcal{F}_p(\mathbf{r})$  will be presented later. To further simplify our analysis, we assume here that the UP dispersion does not get populated by parametric scattering processes and thus, by means of the Hopfield coefficients  $2X_{\mathbf{k}}^2, 2C_{\mathbf{k}}^2 = 1 \pm (\omega_{\mathbf{k}}^C - \omega_{\mathbf{k}}^X)/\sqrt{(\omega_{\mathbf{k}}^C - \omega_{\mathbf{k}}^X)^2 + \Omega_R^2}$ , we project the GPE (1) onto the LP component<sup>3,31</sup>  $\psi_{\mathbf{k}} = X_{\mathbf{k}}\psi_{X,\mathbf{k}} + C_{\mathbf{k}}\psi_{C,\mathbf{k}}$ , where  $\psi(\mathbf{r}, t) = \sum_{\mathbf{k}} e^{i\mathbf{k} \cdot \mathbf{r}} \psi_{\mathbf{k}}(t)$ :

$$i\partial_t \psi_{\mathbf{k}} = \left[ \omega_{\mathbf{k}}^{LP} - i\frac{\gamma_{\mathbf{k}}}{2} \right] \psi_{\mathbf{k}} + C_{\mathbf{k}} \sum_{\mathbf{q}} C_{\mathbf{q}} V_d(\mathbf{k} - \mathbf{q}) \psi_{\mathbf{q}} + \sum_{\mathbf{k}_1, \mathbf{k}_2} g_{\mathbf{k}, \mathbf{k}_1, \mathbf{k}_2} \psi_{\mathbf{k}_1 + \mathbf{k}_2 - \mathbf{k}}^* \psi_{\mathbf{k}_1} \psi_{\mathbf{k}_2} + \tilde{f}_p(t) \delta_{\mathbf{k}, \mathbf{k}_p}. \quad (3)$$

Here,  $\gamma_{\mathbf{k}} = \gamma_X X_{\mathbf{k}}^2 + \gamma_C C_{\mathbf{k}}^2$  is the effective LP decay rate, the interaction strength is given by  $g_{\mathbf{k},\mathbf{k}_1,\mathbf{k}_2} = g_X X_{\mathbf{k}} X_{\mathbf{k}_1+\mathbf{k}_2-\mathbf{k}} X_{\mathbf{k}_1} X_{\mathbf{k}_2}$ , and the pumping term by  $\hat{f}_p(t) = C_{\mathbf{k}_p} f_p e^{-i\omega_p t}$ .

### III. LINEAR RESPONSE THEORY

In the limit where the homogeneously pumped system is only weakly perturbed by the external potential  $V_d(\mathbf{r})$ , we apply a linear response analysis<sup>32</sup>: The LP field is expanded around the mean-field terms for the three  $n = 1, 2, 3 = s, p, i$  OPO states<sup>33</sup>,

$$\psi_{\tilde{\mathbf{k}}} = \sum_{n=1}^3 e^{-i\omega_n t} \left[ \psi_n \delta_{\tilde{\mathbf{k}},0} + u_{n,\tilde{\mathbf{k}}} e^{-i\omega t} + v_{n,-\tilde{\mathbf{k}}}^* e^{i\omega t} \right], \quad (4)$$

where  $\tilde{\mathbf{k}} = \mathbf{k} - \mathbf{k}_n$ . Eq. (3) is expanded linearly in both the fluctuations terms,  $u_{n,\tilde{\mathbf{k}}}$  and  $v_{n,\tilde{\mathbf{k}}}$ , as well as the defect potential. At zero-th order, the three complex uniform mean-field equations can be solved to obtain the dependence of the signal, pump and idler energy blue-shifts,  $\epsilon_n = g_X X_{\mathbf{k}_n}^2 |\psi_n|^2$  on the system parameters<sup>31,34</sup>. A typical behaviour of  $\epsilon_n$  as a function of the rescaled pump intensity  $I_p = g_X C_{\mathbf{k}_p}^2 f_p^2 / X_{\mathbf{k}_p}^2$  in the optical limiter regime is plotted in the left panel of Fig. 1. At first order, one obtains six coupled equations diagonal in momentum space<sup>18</sup>

$$\omega \mathbf{w}_{\tilde{\mathbf{k}}} = \mathcal{L}_{\tilde{\mathbf{k}}} \mathbf{w}_{\tilde{\mathbf{k}}} + \frac{1}{2} \Psi_d, \quad (5)$$

for the 6-component vector  $\mathbf{w}_{\tilde{\mathbf{k}}} = (u_{n,\tilde{\mathbf{k}}}, v_{n,\tilde{\mathbf{k}}})^T$  and for the potential part,  $\Psi_d = (\psi_n C_{\mathbf{k}_n} C_{\mathbf{k}+\mathbf{k}_n} V_d(\mathbf{k}), -\psi_n^* C_{\mathbf{k}_n}^* C_{\mathbf{k}_n-\mathbf{k}} V_d(-\mathbf{k}))^T$ . In (5) we have only kept the terms oscillating at the frequencies  $\omega_n \pm \omega$  and neglected the other terms in the expansion (i.e.,  $2\omega_n - \omega_m \pm \omega$ ), which are oscillating at frequencies far from the LP band, and thus with negligible amplitudes. In the particle-like and the hole-like channels, the Bogoliubov matrix determining the spectrum of excitations can be written as<sup>18</sup>

$$\mathcal{L}_{\mathbf{k}} = \begin{pmatrix} M_{\mathbf{k}} & Q_{\mathbf{k}} \\ -Q_{-\mathbf{k}}^* & -M_{-\mathbf{k}}^* \end{pmatrix}, \quad (6)$$

where the 3 OPO states components are

$$(M_{\mathbf{k}})_{mn} = \left[ \omega_{\mathbf{k}_m+\mathbf{k}}^{LP} - \omega_m - i \frac{\gamma_{\mathbf{k}_m+\mathbf{k}}}{2} \right] \delta_{m,n} \quad (7)$$

$$+ 2 \sum_{q,t=1}^3 g_{\mathbf{k}_m+\mathbf{k},\mathbf{k}_n+\mathbf{k},\mathbf{k}_t} \psi_q^* \psi_t \delta_{m+q,n+t}$$

$$(Q_{\mathbf{k}})_{mn} = \sum_{q,t=1}^3 g_{\mathbf{k}_m+\mathbf{k},\mathbf{k}_q,\mathbf{k}_t} \psi_q \psi_t \delta_{m+n,q+t}. \quad (8)$$

In absence of a defect potential ( $\Psi_d = 0$ ), Eq. (5) is the eigenvalue equation for the spectrum of excitations of a

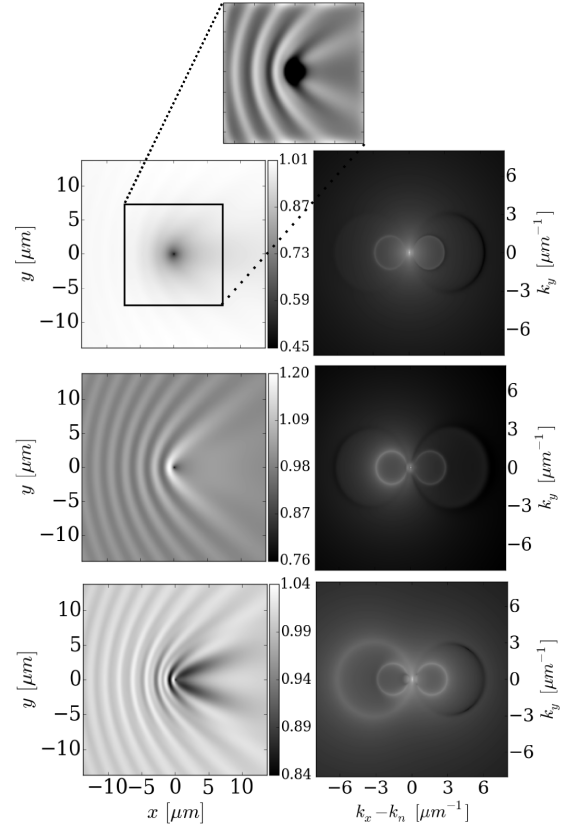


FIG. 2. Linear responses to a static defect of the three OPO states in real and momentum space. Rescaled filtered OPO emissions (signal [top panels], pump [middle], and idler [bottom]) in real space  $|\psi(\mathbf{r}, \omega_n)|^2 / |\psi_n|^2$  (left panels in linear scale) and momentum space  $|\psi_{\tilde{\mathbf{k}}}(\omega_n)|^2$  (right panel in logarithmic scale) obtained within the linear response approximation. The parameters are the same ones of Fig. 1. For the top left panel of the signal emission in real space, Gaussian filtering is applied to enhance the short wavelength modulations, which amplitudes are otherwise roughly 1% of the average signal intensity and about a factor of 10 times weaker than the modulation amplitudes in the pump fluid.

homogeneous OPO, i.e.,  $\det(\mathcal{L}_{\tilde{\mathbf{k}}} - \omega) = 0$ . The spectrum has 6 branches,  $\omega_{n,(u,v),\tilde{\mathbf{k}}}$ , labeled by  $n = s, p, i$  and  $(u, v)$ . Even though these degrees of freedom are mixed together, at large momenta, one recovers the LP dispersions shifted by the three states energies and momenta, i.e.,:

$$\lim_{\tilde{\mathbf{k}} \gg \sqrt{2m_C \Omega_R}} \omega_{n,(u,v),\tilde{\mathbf{k}}} = \pm (\omega_{\mathbf{k}-\mathbf{k}_n}^{LP} - \omega_n), \quad (9)$$

where + (−) corresponds to the  $u$  ( $v$ ) particle- (hole-)like branch. The OPO solution is stable (shaded area in Fig. 1) as far as  $\Im \omega_{n,(u,v),\tilde{\mathbf{k}}} < 0$ .

The shape of the patterns, or Cherenkov-like waves, resulting from the elastic scattering of the OPO 3-fluids against the static ( $\omega = 0$ ) defect can be determined starting from the spectrum, and in particular evaluating the closed curves  $\Gamma_{n,(u,v),\tilde{\mathbf{k}}}$  in  $\mathbf{k}$ -space, or “Rayleigh rings”<sup>35</sup> defined by condition  $\Re \omega_{n,(u,v),\tilde{\mathbf{k}}} = 0$ <sup>36</sup>. The modu-

lations propagate with a direction  $\hat{\eta}_{n,(u,v),\tilde{\mathbf{k}}}$  orthogonal to each curve  $\Gamma_{n,(u,v),\tilde{\mathbf{k}}}$ , a pattern wavelength given by the corresponding  $|\tilde{\mathbf{k}}|$ , and a group velocity  $\mathbf{v}_{n,(u,v),\tilde{\mathbf{k}}}^{(g)} = \nabla_{\tilde{\mathbf{k}}} \Re \omega_{n,(u,v),\tilde{\mathbf{k}}}$ , where  $\xi_{n,(u,v),\tilde{\mathbf{k}}} = |\mathbf{v}_{n,(u,v),\tilde{\mathbf{k}}}^{(g)}| \Im \omega_{n,(u,v),\tilde{\mathbf{k}}}$  determines the distance, at any given direction  $\hat{\eta}_{n,(u,v),\tilde{\mathbf{k}}}$ , over which the perturbation extends away from the defect. For a single fluid under a coherent pump, the qualitative shape of the modulation pattern generated in the fluid by the defect is mostly determined by the excitation spectrum<sup>37,38</sup>.

For OPO, the spectrum of excitation on top of each of the three,  $n = 1, 2, 3$ , states (see<sup>34</sup>) generates six identical Rayleigh rings  $\Gamma_{n,(u,v),\tilde{\mathbf{k}}}$  for the 3 states. The Rayleigh rings for the OPO conditions specified in Fig. 1 are clearly visible in the right panels of Fig. 2, where we plot the  $\mathbf{k}$ -space photoluminescence filtered at each state energy, i.e.,  $|\psi_{\tilde{\mathbf{k}}}(\omega_n)|^2 = |\psi_n \delta_{\tilde{\mathbf{k}},0} + u_{n,\tilde{\mathbf{k}}} + v_{n,-\tilde{\mathbf{k}}}^*|^2$ . We have here chosen a  $\delta$ -like defect potential,  $V_d(\mathbf{k}) = g_d$ , but we have however checked that our results do not depend on its exact shape<sup>34</sup>. For the OPO conditions considered here, the signal momentum is at  $k_s \simeq 0$ , and thus only four of the six rings are present. The same rings are also plotted in the right panel of Fig. 1, shifted at each of the three OPO state momentum  $\mathbf{k}_n$ ,  $\Gamma_{n,(u,v),\tilde{\mathbf{k}}+\mathbf{k}_n}$  and energies  $\omega_n$ . It is important to note that, even though the three OPO states have locked responses because the three states display the same spectrum of excitations, only one of the rings  $\Gamma_{n,(u,v),\tilde{\mathbf{k}}+\mathbf{k}_n}$  is the most resonant at  $\omega_n$  with the interaction blue-shifted lower polariton dispersion,

$$\bar{\omega}_{\tilde{\mathbf{k}}}^{LP} = \omega_{\tilde{\mathbf{k}}}^{LP} + 2X_{\tilde{\mathbf{k}}}^2 \sum_{n=1}^3 \epsilon_n, \quad (10)$$

where  $\epsilon_n = g_X X_{\tilde{\mathbf{k}}_n}^2 |\psi_n|^2$  are the mean-field energy blue-shifts (measured in Fig. 1 in units of  $\gamma_p = \gamma_{\mathbf{k}_p}$ ). This implies that the most visible modulation for each fluid should be the most resonant one, with superimposed weaker modulations coming from the other two state rings.

In the specific case of Fig. 1, the signal is at  $k_s \simeq 0$  and thus produces no rings in momentum space. The other four rings are very far from being resonant with the blue-shifted LP dispersion (10) at  $\omega_s$ , and thus the signal displays only an extremely weak modulation coming from the next closer ring, which is the one associated with the pump state,  $\Gamma_{p,u,\tilde{\mathbf{k}}+\mathbf{k}_s}$ . We estimate that the signal modulation amplitudes are roughly 1% of the average signal intensity and about a factor of 10 times weaker than the modulation amplitudes in the pump fluid. In order to show that the signal has weak modulations coming from the pump, we apply a Gaussian filter to the real space images (see inset of the left top panel of Fig. 2). As explained in more details in<sup>34</sup>, Gaussian filtering consists of subtracting from the original data a copy which has been convoluted with a Gaussian kernel, thus getting rid

of the long-wavelength modulations. This procedure reveals that indeed the pump imprints its modulation also into the signal, even though these are extremely weak, thus leaving the signal basically insensitive to the presence of the defect.

Pump and idler states are each mostly resonant with their own rings, i.e.,  $\Gamma_{p,u,\tilde{\mathbf{k}}+\mathbf{k}_p}$  at  $\omega_p$  and  $\Gamma_{i,u,\tilde{\mathbf{k}}+\mathbf{k}_i}$  at  $\omega_i$ , respectively. Thus one should then observe two superimposed modulations in both pump and idler filtered emissions, the stronger one for each being the most resonant one. However, the modulations associated to the idler only propagate very close to the defect, at an average distance  $\xi_{i,u,\tilde{\mathbf{k}}} \sim 1.7 \mu\text{m}$  before getting damped, and thus are not clearly visible. For the OPO conditions considered, this is due to the small idler group velocity  $\mathbf{v}_{i,u,\tilde{\mathbf{k}}}^{(g)}$ , as the dispersion is almost excitonic at the idler energy.

We can conclude that, for the typical OPO condition with a signal at  $k_s \simeq 0$ , considered in Figs. 1 and 2, the signal fluid does not show modulations and the extremely weak scattering inherited from the pump state can be appreciated only after a Gaussian filtering procedure of the image. In contrast, the idler has a locked response to the one of the pump state. Note that, for the conditions shown in Fig. 1, as well as the other cases considered in Ref.<sup>34</sup>, the subsonic to supersonic crossover of the pump-only state<sup>25</sup> happens well above the region of stability of OPO. Thus it is not possible to study a case where the pump is already subsonic and at the same time promotes stimulated scattering.

#### IV. EXPERIMENTS

We now turn to the experimental analysis. We use a continuous-wave laser to drive a high quality ( $Q = 14000$ ) GaAs microcavity sample into the OPO regime — details on the sample can be found in a previous publication<sup>39,40</sup>. The polariton dispersion is characterised by a Rabi splitting  $\Omega_R = 5.4 \text{ meV}$ , the exciton energy  $\omega_0^X = 1485.26 \text{ meV}$  and we choose a sample region where the cavity-exciton detuning is slightly negative,  $-1 \text{ meV}$ . We pump at  $k_p = 0.89 \mu\text{m}^{-1}$  and  $\omega_p - \omega_0^X = -2.43 \text{ meV}$ , and, at pump powers 1.5-times above threshold, we obtain an OPO with signal at small wavevector  $k_s = 0.21 \mu\text{m}^{-1}$  and  $\omega_s - \omega_0^X = -2.95 \text{ meV}$ , and idler at  $k_i = 1.57 \mu\text{m}^{-1}$  and  $\omega_i - \omega_0^X = -1.91 \text{ meV}$ . The defect we use in the sample is a localized inhomogeneity naturally present in the cavity mirror. Note that the exact location of the defect can be extracted from the emission spectrum and is indicated with a dot (orange) symbol in the profiles of Fig. 3.

In order to filter the emission at the three states energies,  $I_{s,p,i}(\mathbf{r} = x, y)$ , and obtain 2D spatial maps for the OPO three states, we use a spectrometer and, at a fixed position  $x_0$ , obtain the intensity emission as a function of energy and position,  $I(\epsilon, x_0, y)$ . By changing  $x_0$  we build the full emission spectrum as a function

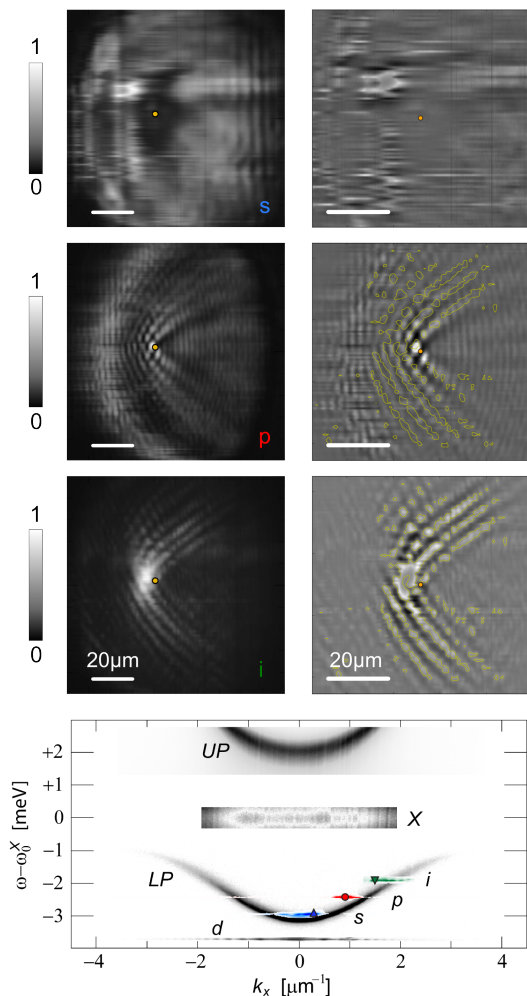


FIG. 3. (Color online) Experimental OPO spectrum and filtered emissions of signal, pump and idler in presence of a structural defect. The six panels show the filtered emission profiles in real space of signal (top), pump (middle) and idler (bottom)  $I_{s,p,i}(\mathbf{r})$ . A Gaussian filtering to enhance the short wavelength modulations is applied in the right column panels. Here, the extracted wave-crests from the idler emission (yellow contours in the bottom panel) are also superimposed to the pump profile (middle) by applying a  $\pi$ -phase shift. The (orange) dot indicates the position of the defect. The lower panel shows the experimental OPO spectrum. Energy and momentum of the three OPO states are labeled with a [blue] upper triangle (signal), a [red] circle (pump), and a [green] lower triangle (idler), while the localised state, clearly visible just below the bottom of the LP dispersion, is indicated with the symbol  $d$ . The bare LP dispersion is extracted from an off-resonant low pump power measurement, as well as the emission of the exciton reservoir (X) and the one of the UP dispersion (each in a different scale).

of energy and 2D position,  $I(\epsilon, \mathbf{r})$ . The filtered emission for each OPO state is obtained from the integrals  $I_{n=s,p,i}(\mathbf{r}) = \int_{\omega_n - \sigma}^{\omega_n + \sigma} d\epsilon I(\epsilon, \mathbf{r})$ , with  $\sigma = 0.08$  meV. The results are shown in Fig. 3 for respectively the signal (top panel), pump (middle) and the idler (bottom) pro-

files. The signal profile shows no appreciable modulations around the defect locations, nor these could be observed after applying a Gaussian filtering procedure of the image. In contrast, in agreement with the theoretical results, both filtered profiles of pump and idler show the same Cherenkov-like pattern. We extract the wave-crests from the idler profile ([yellow] contours in the bottom panel) and superimpose them to the pump profile (middle panel) with an added  $\pi$ -phase-shift, revealing that the only modulations visible in the idler state are the ones coming from the pump state.

## V. NUMERICAL ANALYSIS

The agreement between the results obtained experimentally and within the linear response approximation is additionally confirmed by an exact full numerical analysis of the coupled equations (1) for a finite size pump via a 5<sup>th</sup>-order adaptive-step Runge-Kutta algorithm. Details are given in<sup>34</sup>. The pumping conditions are very similar to those previously considered in the linear response approximation of Figs. 1 and 2, while the pump profile  $\mathcal{F}_p(\mathbf{r})$  is now finite-size top-hat. In particular, we consider the case of zero cavity-exciton detuning,  $k_p = 1.6 \mu\text{m}^{-1}$ ,  $\omega_p - \omega_X^0 = -0.44$  meV and the pump power strength is fixed just above threshold, so that to produce a stable steady state OPO with, in absence of the defect, signal at small wavevector  $k_s = -0.2 \mu\text{m}^{-1}$  and idler at  $k_i = 3.4 \mu\text{m}^{-1}$ .

When adding a localised defect potential, the steady state OPO develops Rayleigh rings in momentum space, yet, as shown in<sup>34</sup>, the spectrum continues to be  $\delta$ -like in energy, allowing to easily filter in energy the emission of the three OPO states. Results are shown in Fig. 4, where real-space emissions  $|\psi_C(\mathbf{r}, \omega_n)|^2$  are plotted in the left panels, while the ones in momentum space  $|\psi_C(\tilde{\mathbf{k}}, \omega_n)|^2$  in the right panels. We observe a very similar phenomenology to that one obtained in the linear approximation shown in Fig. 2. The signal now is at slightly negative values of momenta  $k_s = -0.2 \mu\text{m}^{-1}$ , thus implying a very small Rayleigh ring associated with this state. Thus we observe that only the modulations associated with the pump are the ones that are weakly imprinted in the signal state and that can be observed by means of a Gaussian filtering (inset of top-left panel). We have fitted the upstream wave-crests and obtained the same modulation wave-vector as the pump one ([blue] upper triangles). Similarly to the linear response case, we also find here that the most visible perturbation in the emission filtered at the idler energy is the one due to the pump Rayleigh ring. As before, the modulations due to the idler Rayleigh ring cannot propagate far from the defect because of the small group velocity associated with this state.

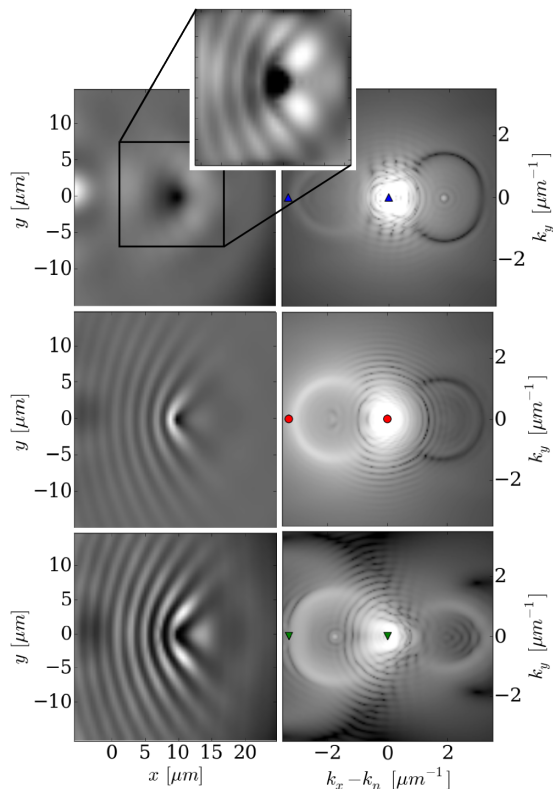


FIG. 4. (Color online) Full numerical responses to a static defect of the three OPO states in real and momentum space. Filtered OPO emissions (signal [top panels], pump [middle], and idler [bottom]) in real space  $|\psi_C(\mathbf{r}, \omega_n)|^2$  (left panels in linear scale) and momentum space  $|\psi_C(\mathbf{k}, \omega_n)|^2$  (right panel in logarithmic scale) obtained by a full numerical evaluation of (1). For the top left panel of the signal space emission, Gaussian filtering is applied to enhance the short wavelength modulations of this state, revealing that the modulations corresponding to the pump state are also imprinted (though weakly) into the signal. The symbols indicate the pump ring diameter extracted from fitting the upstream modulations and resulting in a density wave wave-vector coinciding with the one of the pump  $k_p = 1.6 \mu\text{m}^{-1}$ .

## VI. CONCLUSIONS

To conclude, we have reported a joint theoretical and experimental study of the superfluid properties of a non-equilibrium condensate of polaritons in the so-called optical parametric oscillator configuration by studying the scattering against a static defect. We have found that while the signal is basically free from modulations, pump and idler lock to the same response. We have highlighted the role of the coupling between the OPO components by non-linear and parametric processes. These are responsible for the transfer of the spatial modulations from one component to the other. This process is most visible in the clear spatial modulation pattern that is induced by the non-superfluid pump onto the idler, while the same modulations are only extremely weakly transferred into

the signal, because of its low characteristic wavevector, so much that experimentally cannot be resolved. The main features of the real- and momentum-space emission patterns are understood in terms of Rayleigh scattering rings for each component and a characteristic propagation length from the defect; the rings are then transferred to the other components by nonlinear and parametric processes. Our theoretical and experimental results stress the complexities and richness involved when looking for superfluid behaviours in non-equilibrium multicomponent condensates such as the ones obtained in the optical parametric oscillation regime.

## ACKNOWLEDGMENTS

We are grateful to M. Wouters, C. Tejedor and M. De Giorgi for stimulating discussions. Financial support from the ERC POLAFLOW (grant n. 308136) is acknowledged. FMM acknowledges financial support from the Ministerio de Economía y Competitividad (MINECO, contract No. MAT2011-22997), the Comunidad Autonoma de Madrid (CAM, contract No. S-2009/ESP-1503), and the European Science Foundation (ESF) program Intelbiomat. IC acknowledges financial support by the ERC through the QGBE grant and by the Autonomous Province of Trento, partly through the “On silicon chip quantum optics for quantum computing and secure communications” (“SiQuro”). MHS acknowledges support from EPSRC (grants EP/I028900/2 and EP/K003623/2).

# Supplemental Material for “On multicomponent polariton superfluidity in the optical parametric oscillator regime”

In the manuscript, we carry on a theoretical and experimental analysis of the response of microcavity polaritons in the optical parametric oscillator (OPO) regime to a static defect. For the theoretical calculations we follow two independent approaches: In the first approach, we exactly numerically solve the dynamics of the two coupled Gross-Pitaevskii equations (GPEs) for the exciton and cavity fields for the realistic case of a finite-size top-hat pump profile  $\mathcal{F}_p(\mathbf{r})$ . In the second approach, we apply a perturbative linear response approximation for the lower polariton (LP) state which leads to semi-analytical results in the limiting case of a spatially homogeneous pump profile. Both methods have been already successfully used in the literature to explore several properties of the OPO operation.

While all fundamental formulae and information has been given in the main text, in this Supplementary Material (SM) we present some additional details on both approaches that might be of interest to the specialized reader. In addition to that, we make use of the linear response approach to examine some regimes that are hardly accessed experimentally or within a full numerical approach, which however allow to put the conclusions of our work into a broader perspective.

## VII. FULL NUMERICS

The classical driven-dissipative non-linear Gross-Pitaevskii equation (GPE) for the coupled exciton and cavity fields  $\psi_{X,C}(\mathbf{r}, t)$  ( $\hbar = 1$ )

$$i\partial_t \begin{pmatrix} \psi_X \\ \psi_C \end{pmatrix} = \hat{H} \begin{pmatrix} \psi_X \\ \psi_C \end{pmatrix} + \begin{pmatrix} 0 \\ F_p(\mathbf{r}, t) \end{pmatrix}, \quad (1)$$

where

$$\hat{H} = \begin{pmatrix} \omega_{-i\nabla}^X - i\frac{\gamma_X}{2} + g_X|\psi_X|^2 & \Omega_R/2 \\ \Omega_R/2 & \omega_{-i\nabla}^C - i\frac{\gamma_C}{2} + V_d \end{pmatrix}, \quad (2)$$

is solved numerically on a 2D grid of  $N \times N = 2^8 \times 2^8$  points and a separation of  $0.47 \mu\text{m}$  (i.e., in a box  $L \times L = 121 \mu\text{m} \times 121 \mu\text{m}$ ) by using a 5<sup>th</sup>-order adaptive-step Runge-Kutta algorithm. Convergence has been checked both with respect the resolution in space  $L/N$  as well as in momentum  $\pi/L$ , without<sup>20,21</sup> as well as in presence of the defect. The same approach has been already used in previous publications from some of the authors (for a review, see Refs.<sup>20,21</sup>). As for the system parameters, we have considered a LP dispersion at zero photon-exciton detuning,  $\omega_0^C = \omega_0^X$ , a dispersionless excitonic spectrum,  $\omega_{\mathbf{k}}^X = \omega_0^X$  and a quadratic dispersion for photons  $\omega_{\mathbf{k}}^C = \omega_0^C + k^2/2m_C$ , with the photon mass  $m_C = 2.3 \times 10^{-5}m_e$ , where  $m_e$  is the bare electron mass. The LP dispersion,

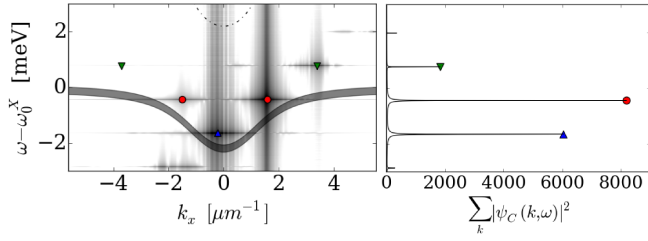
$2\omega_{\mathbf{k}}^{LP} = \omega_{\mathbf{k}}^C + \omega_{\mathbf{k}}^X - \sqrt{(\omega_{\mathbf{k}}^C - \omega_{\mathbf{k}}^X)^2 + \Omega_R^2}$  is characterised by a Rabi splitting  $\Omega_R = 4.4 \text{ meV}$ . Further, the exciton and cavity decay rates are fixed to  $\gamma_X = \gamma_C = 0.53 \text{ meV}$ . For the defect we choose a  $\delta$ -like defect potential

$$V_d(\mathbf{r}) = g_d\delta(\mathbf{r} - \mathbf{r}_0), \quad (3)$$

where its location  $\mathbf{r}_0$  is fixed at one of the  $N \times N$  points of the grid. Note that in a finite-size OPO, local currents lead to inhomogeneous OPO profiles in within the pump spot, despite the external pump having a top-hat profile with a completely flat inner region<sup>20,21</sup> — as shown later, this can be observed in the filtered OPO profiles evaluated in absence of a defect shown as dashed lines in S. Fig. 2. We have thus chosen the defect location so that it lies in the smoothest and most homogeneous part of the OPO profiles.

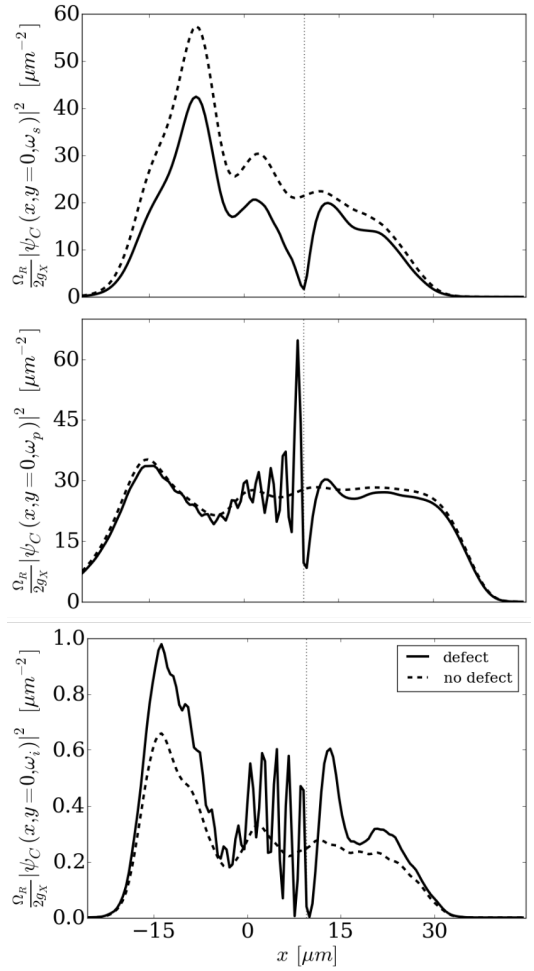
Also we have checked that our results do not qualitatively depend on the strength  $g_d$  (nor on the sign) of the defect potential, as far as this does not exceed a critical value above which it destabilises the OPO steady-state regime. The pump,  $F_p(\mathbf{r}, t) = \mathcal{F}_p(\mathbf{r})e^{i(\mathbf{k}_p \cdot \mathbf{r} - \omega_p t)}$ , has a smoothen and rotationally symmetric top-hat profile,  $\mathcal{F}_p(\mathbf{r}) = \mathcal{F}_p(r) = \frac{f_p}{2} [\tanh(\frac{r+\sigma_p}{r_0}) - \tanh(\frac{r-\sigma_p}{r_0})]$  with strength  $f_p = 1.23f_p^{\text{th}} = 0.053 \text{ meV}/\mu\text{m}$  and parameters  $r_0 = 8.68 \mu\text{m}$ ,  $\sigma_p = 34.72 \mu\text{m}$ . We pump at  $k_p = 1.6 \mu\text{m}^{-1}$  in the  $x$ -direction,  $\mathbf{k}_p = (k_p, 0)$ , and at  $\omega_p - \omega_X^0 = -0.44 \text{ meV}$ , i.e., roughly  $0.5 \text{ meV}$  above the bare LP dispersion. By increasing the pump strength  $f_p$ , we find the threshold  $f_p^{\text{th}}$  above which OPO switches on, leading to two conjugate signal and idler states. We then fix the pump strength just above this threshold ( $f_p = 1.23f_p^{\text{th}}$ ), where we find a steady state OPO solution which is stable (see Ref.<sup>21</sup> for further details). In absence of the defect, this condition corresponds to a signal state at  $k_s = -0.2 \mu\text{m}^{-1}$  and  $\omega_s - \omega_X^0 = -1.64 \text{ meV}$  and an idler at  $k_i = 3.4 \mu\text{m}^{-1}$  and  $\omega_i - \omega_X^0 = 0.76 \text{ meV}$ . It is interesting to note that already very close to the lower pump power threshold for OPO, the selected signal momentum is very close to zero. This contrasts with what one obtains in the linear approximation scheme, where instead just above the lower OPO threshold there exists a broad interval of permitted values for  $k_s$  (and thus  $k_i$ ) — we will discuss further this “selection problem” for parametric scattering later in the section “Linear response”.

We evaluate the time dependent full numerical solution of (1)  $\psi_{X,C}(\mathbf{r}, t)$ , until a steady state regime is reached. Here, both its Fourier transform to momentum  $\mathbf{k}$  and energies  $\omega$  can be evaluated numerically. We plot on the left panel of S. Fig. 1 a cut at  $k_y = 0$  of the photonic component of the OPO spectrum in presence of a point-like defect,  $|\psi_C(k_x, 0, \omega)|^2$ , as a function of the rescaled energy  $\omega - \omega_X^0$  versus the  $x$ -component of mo-



S. FIG. 1. (Color online) OPO spectrum obtained by full numerics. Left panel: Photonic component of the OPO spectrum in presence of a point-like defect,  $|\psi_C(k_x, 0, \omega)|^2$  (logarithmic scale), as a function of the rescaled energy  $\omega - \omega_0^X$  versus the  $x$ -component of momentum  $k_x$  (cut at  $k_y = 0$ ) for a top-hat pump (see text for the space profile and parameter values), with intensity  $f_p = 1.23 f_p^{\text{th}}$  above the OPO threshold, pump wave-vector  $k_p = 1.6 \mu\text{m}^{-1}$  in the  $x$ -direction and  $\omega_p - \omega_0^X = -0.44 \text{ meV}$ . The symbols indicate the signal ([blue] upper triangle), pump ([red] circle), and idler ([green] lower triangle) energies, as well as the two momenta  $k_x$  on each state Rayleigh ring at  $k_y = 0$ . Note that the logarithmic scale results in a fictitious broadening in energy of the spectrum, which is in reality  $\delta$ -like (see right panel). The bare LP dispersion, including its broadening due to finite lifetime, is plotted as a shaded grey region, while the bare UP dispersion as a (black) dot-dashed line. Right panel: Momentum integrated spectrum,  $\sum_{\mathbf{k}} |\psi_C(\mathbf{k}, \omega)|^2$  (linear scale) as a function of the rescaled energy  $\omega - \omega_0^X$ , where it can be clearly appreciated that the emission is  $\delta$ -like in energy.

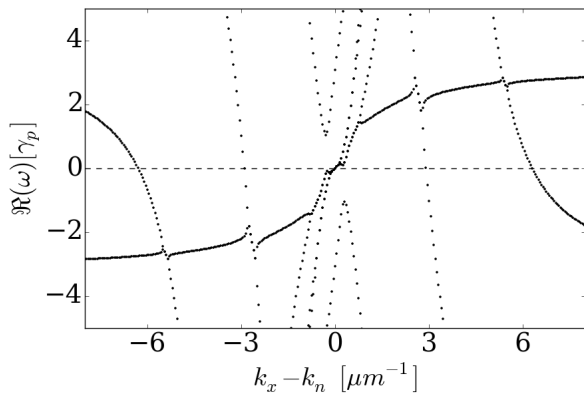
momentum  $k_x$  (cut at  $k_y = 0$ ). In the right panel we plot instead the corresponding momentum integrated spectrum,  $\sum_{\mathbf{k}} |\psi_C(\mathbf{k}, \omega)|^2$ . Here, we can clearly see that the presence of the defect does not modify the fact that the OPO emission for the OPO signal ([blue] upper triangle), pump ([red] circle), and idler ([green] lower triangle) states has a completely flat dispersion in energy, thus indicating that a stable steady state OPO solution has been reached. Note that in the spectrum map of the left panel of Fig. 1, the logarithmic scale results in a fictitious broadening in energy. However, from the integrated spectrum plotted in linear scale in the right panel of Fig. 1 one can clearly appreciate that this emission is  $\delta$ -like, exactly as it happens for the homogeneous OPO case<sup>21</sup>. Thus the effect of the defect is to induce only elastic (i.e., at the same energy) scattering; now the three OPO states emit each on its own Rayleigh ring (given each by the symbols on the left panel of S. Fig. 1 which represent the rings at a cut for  $k_y = 0$ ). This makes it rather difficult to extract the separated signal, pump and idler profiles by filtering in momentum, as done previously for the homogeneous case, but it still allows to filter those profiles very efficiently in energy. In fact, because the emission is  $\delta$ -like, it is enough to fix a single value of the energy  $\omega$  to the one of the three states  $\omega_{n=s,p,i}$ , thus extracting the filtered profiles either in real space  $|\psi_C(\mathbf{r}, \omega_n)|^2$  or in momentum space  $|\psi_C(\mathbf{k}, \omega_n)|^2$  — we have however checked that integrating in a narrow energy window around  $\omega_n$  does not quantitatively change the results.



S. FIG. 2. Real space signal, pump and idler OPO one-dimensional filtered profiles derived from finite size numerics with and without a defect. Rescaled OPO filtered emissions along the  $y = 0$  direction,  $|\psi_C(x, y = 0, \omega_n)|^2 \frac{\Omega_R}{2g_X}$ , obtained by numerically solving the GPE Eq. (1) of the main manuscript. While the dashed lines represent the filtered emissions of signal (top panel), pump (middle) and idler (bottom) for a top-hat pump without a defect, the solid lines are the same OPO conditions but now for a defect positioned at  $(x_d, y_d) = (9.5, -0.5) \mu\text{m}$  corresponding to the vertical dotted lines. The system parameters are the same ones as those of Fig. 4 of the main manuscript.

The results of the above described filtering are shown in Fig. 4 of the manuscript. In S. Fig. 2 we instead plot the corresponding one-dimensional profiles in the  $y = 0$  direction both in presence (solid line) and without (dashed line) a defect. Here, we can observe that, even if the pump has a top-hat flat profile, as also commented previously, in absence of a defect, the finite-size OPO is characterised by inhomogeneous profiles of signal, pump and idler because of localised currents. Further, we observe that the presence of a defect induces strong modulations in pump and idler. In order to reveal that the pump also imprints its modulation into

the signal, even though these are extremely weak (and hardly visible in both the top main panel of Fig. 4 of the manuscript and the top panel of S. Fig. 2), we apply a Gaussian filtering to the signal images, which result is shown in the inset of the top-left panel of Fig. 4 in the manuscript. This consists of the following procedure. The original data for the real space profile  $\psi(\mathbf{r})$  are convoluted with a Gaussian kernel  $K(\mathbf{r} - \mathbf{r}')$ , obtaining a new profile,  $\tilde{\psi}(\mathbf{r}') = \int d\mathbf{r} \psi(\mathbf{r}) K(\mathbf{r} - \mathbf{r}')$ , where short wavelength features are smoothen out. The convoluted image  $\tilde{\psi}(\mathbf{r}')$  is then subtracted from the original data, giving  $\psi(\mathbf{r}) - \tilde{\psi}(\mathbf{r})$ , and effectively filtering out all long wavelength details. The same procedure of Gaussian filtering is also applied to the signal emission profile obtained within the linear response analysis and shown in the inset of the top left panel of Fig. 2 of the manuscript.

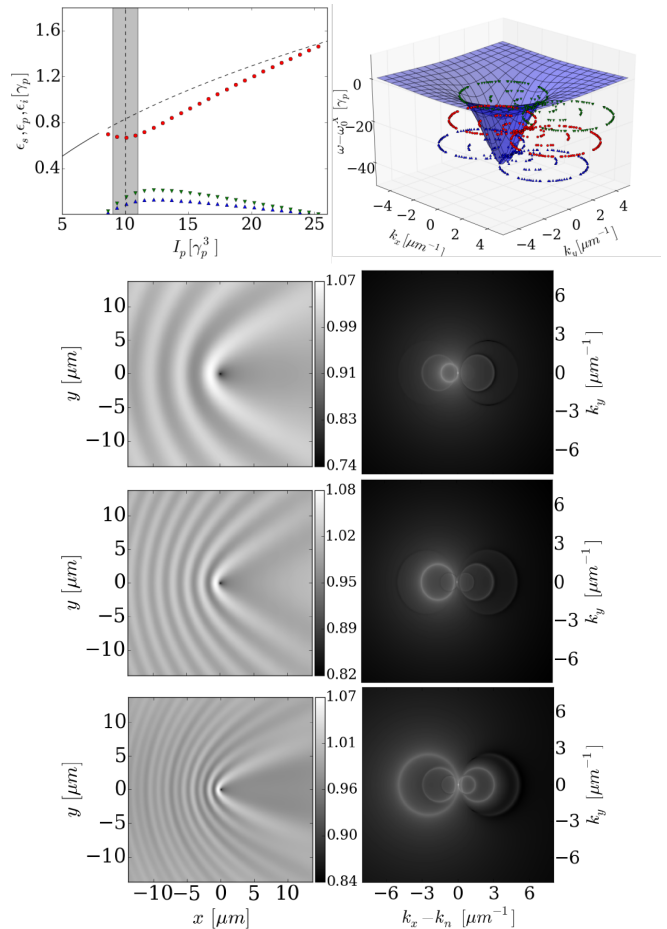


S. FIG. 3. Spectrum of collective excitations. Cut at  $k_y = 0$  of the real part of the quasiparticle energy dispersion  $\Re\omega_{n,(u,v),\mathbf{k}-\mathbf{k}_n}$  plotted versus  $k_x - k_n$ . The spectrum is evaluated within the linear approximation scheme and the parameters are the same ones used for Fig. 2 of the main manuscript.

### VIII. LINEAR RESPONSE

In the manuscript we also make use of the linear response approximation to analyse the OPO response to a static defect, valid for a homogeneous pump scheme. In order to do so, we first evaluate the Bogoliubov matrix given in Eq. (6) of the manuscript, whose eigenvalues determine the spectrum of collective excitations. We plot in S. Fig. 3 a typical collective dispersion (here we consider the same system parameters as the ones used in Fig. 2 of the manuscript), by plotting the real part of the Bogoliubov matrix eigenvalues  $\Re\omega_{n,(u,v),\mathbf{k}-\mathbf{k}_n}$  as a function of  $k_x - k_n$  (cut at  $k_y = 0$ ). Note that the Rayleigh rings can be found by finding the intersections  $\Re\omega_{n,(u,v),\mathbf{k}-\mathbf{k}_n} = 0$ .

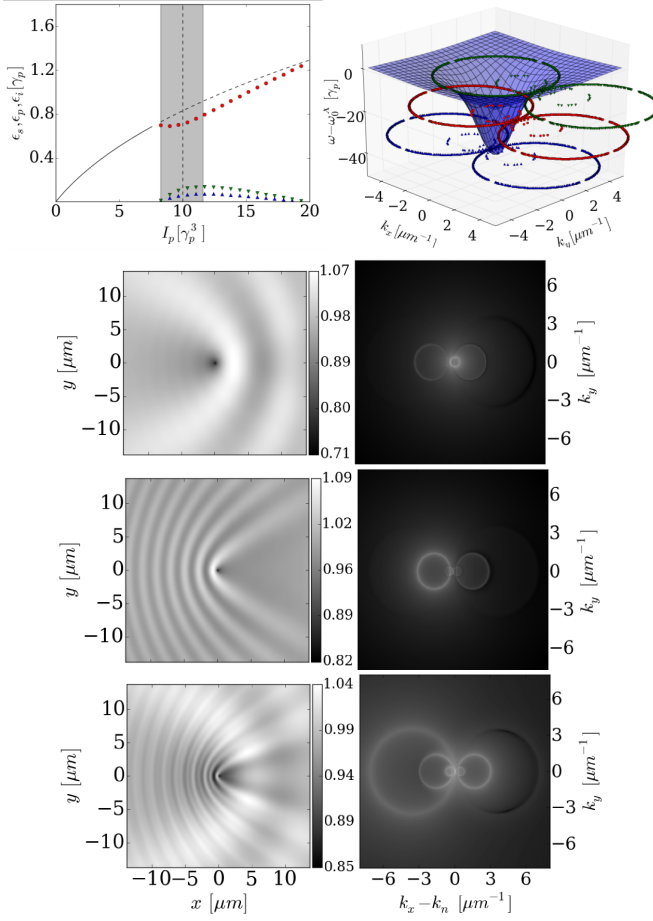
As also done for the full numerics, we consider there a  $\delta$ -like disorder potential  $V_d(\mathbf{r}) = g_d\delta(\mathbf{r} - \mathbf{r}_0)$ , and Figs. 1 and 2 of the manuscript, as well as S. Figs. 4 and 5 below, are plotted for this case. We have however checked



S. FIG. 4. (Color online) OPO for finite and positive signal momentum in the linear response approximation for homogeneous pumping. Rescaled OPO emission within the linear response approximation in real  $|\psi(\mathbf{r}, \omega_n)|^2 / |\psi_n|^2$  (left panels in linear scale) and momentum space  $|\psi_{\mathbf{k}}(\omega_n)|^2$  (right panels in linear scale) filtered at the energies of the three OPO states: signal (top panels), pump (middle), and idler (bottom). The parameters are the same as those used in Fig. 2 of the main manuscript, with the exception of the signal and idler momenta, which are now at  $k_s = 0.7 \mu\text{m}^{-1}$  and  $k_i = 2.5 \mu\text{m}^{-1}$  respectively. Each scale of variation for the profiles is plotted in the color-box next to the left panels. A cut in the  $y = 0$  direction for the three profiles is plotted in the bottom panel of S. Fig. 6.

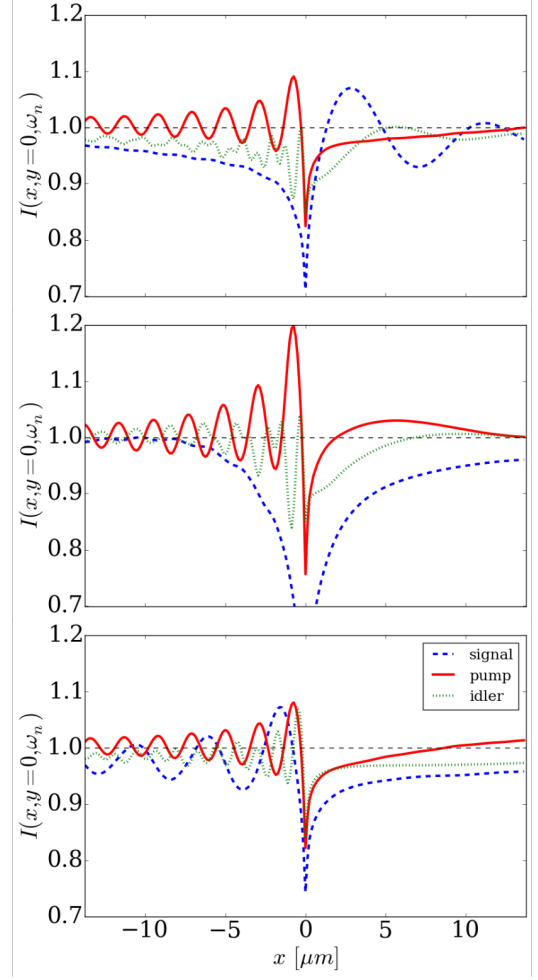
that our results do not depend on the specific shape of the defect potential: In particular we have also considered the response to defects with smoothen Gaussian-like profiles, whose effect is only to partially weaken the upstream modulations emission in real space.

We have seen in the manuscript that both experimentally as well as in the full numerical analysis, one obtains OPO conditions where the signal momentum is very close to zero,  $\mathbf{k}_s \sim 0$ . The reason why OPO selects almost zero momentum signal conditions is still awaiting a theoretical explanation. In contrast, the linear response approximation allows to access very different OPO mean-field



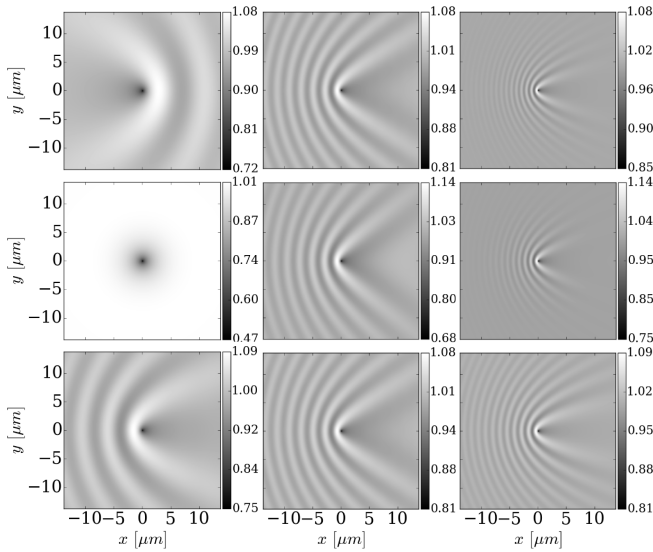
S. FIG. 5. (Color online) OPO for finite and negative signal momentum in the linear response approximation for homogeneous pumping. Rescaled OPO emission within the linear response approximation in real  $|\psi(\mathbf{r}, \omega_n)|^2/|\psi_n|^2$  (left panels in linear scale) and momentum space  $|\psi_{\mathbf{k}}(\omega_n)|^2$  (right panels in linear scale) filtered at the energies of the three OPO states: signal (top panels), pump (middle), and idler (bottom). The parameters are the same as those used in Fig. 2 of the main manuscript, with the exception of the signal and idler momenta, which are now at  $k_s = -0.4 \mu\text{m}^{-1}$  and  $k_i = 3.6 \mu\text{m}^{-1}$  respectively. A cut in the  $y = 0$  direction for the three profiles is plotted in the top panel of S. Fig. 6.

conditions, for which, by leaving unaltered the value of the pump momentum, the signal can appear at finite momentum values, either positive or negative. This is a peculiarity of this approximation scheme, where one can show that, at mean-field level, one has the possibility of choosing different values of the signal momentum  $\mathbf{k}_s$  (and thus the one of the idler  $\mathbf{k}_i$ ), and that this choice range is quite broad particularly when the pump power is close to the lower pump threshold for OPO — the stability region for OPO is plotted as a shaded grey region in the top left panels of S. Figs. 4 and 5. This is a well known “selection problem” for parametric scattering (see Ref.<sup>31</sup>): The reason why in full numerical calculations, parametric scattering processes select a signal with a momentum close



S. FIG. 6. (Color online) Real space signal, pump and idler OPO one-dimensional filtered profiles in the linear response approximation. OPO filtered emissions along the  $y = 0$  direction,  $I(x, y = 0, \omega_n) = |\psi(x, y = 0, \omega_n)|^2/|\psi_n|^2$  rescaled by the mean-field solution  $\psi_n$  in absence of the defect, for the three cases analysed above within the linear response approximation: the case of a signal at  $k_s = -0.4 \mu\text{m}^{-1}$  (top panel) corresponds to the same conditions as S. Fig. 5, a signal at  $k_s = 0.0 \mu\text{m}^{-1}$  (middle panel) corresponds to Fig. 2 of the main manuscript, and a signal at  $k_s = 0.7 \mu\text{m}^{-1}$  (bottom panel) corresponds to S. Fig. 4. In each panel we plot, on the same linear scale, the filtered profiles of signal ([blue] dashed line), pump ([red] solid), and idler ([green] dotted), while the horizontal gray dashed lines represent the values of the mean-field emission prior to adding a defect (rescaled here to 1).

to zero, already very close to the lower pump threshold for OPO, is still awaiting for an explanation. In particular, this quest cannot be addressed within a spatially homogeneous approximation where the three mean-field solutions for pump, signal, and idler states can be describes by plane waves. One can only show that, within the same mean-field approximation scheme, when increasing the pump power towards the upper threshold for OPO, the blue-shift of the LP polariton dispersion due to the



S. FIG. 7. Real space profiles of three uncoupled signal, pump and idler fluids. The rescaled profiles  $|\psi(\mathbf{r}, \omega_n)|^2 / |\psi_n|^2$  are obtained by setting all off-diagonal couplings in Eq. (6) of the main manuscript to zero, resulting in three uncoupled signal (left column), pump (middle column), and idler (right column) fluids. The three rows correspond to the three different cases previously analysed within the linear response approximation: the case of a signal at  $k_s = -0.4 \mu\text{m}^{-1}$  (top row) corresponds to the same conditions as S. Fig. 5, a signal at  $k_s = 0.0 \mu\text{m}^{-1}$  (middle row) corresponds to Fig. 2 of the main manuscript, and a signal at  $k_s = 0.7 \mu\text{m}^{-1}$  (bottom row) corresponds to S. Fig. 4.

increasing mean-field polariton density, causes the signal momentum to converge towards zero<sup>33</sup>  $\mathbf{k}_s \rightarrow 0$ .

*OPO conditions with a finite momentum signal* — Given the freedom of choice for the signal momentum  $\mathbf{k}_s$  close to the lower OPO threshold, we consider here two additional cases, that could not be studied neither experimentally, nor within a full numerical approach, but that instead we can easily analyse within the linear response theory. In particular, we have left fixed the pumping conditions  $k_p = 1.6 \mu\text{m}^{-1}$  and  $\omega_p - \omega_X^0 = -1.25 \text{ meV}$  and considered two opposite situations.

In the first case, the signal has a finite and positive momentum  $k_s = 0.7 \mu\text{m}^{-1}$  and thus the idler is at low momentum,  $k_i = 2.5 \mu\text{m}^{-1}$ . The results are shown in S. Fig. 4. Here we see that all six Rayleigh rings are clearly visible and, in addition, as the idler is at lower momentum compared to the case considered in Figs. 1 and 2 of the manuscript, and thus its dispersion steeper, the idler group velocity is large enough to appreciate the modulation of the Rayleigh ring associated to this state. As a result, each of the three filtered OPO emissions exhibits as the strongest modulation the one coming from its own Rayleigh ring, included the signal which is now at finite and large momentum. In this case, the OPO response of each filtered state profile looks completely independent from the other, as if we were pumping each

state independently.

In the second case shown in S. Fig. 5, the signal is finite and negative,  $k_s = -0.4 \mu\text{m}^{-1}$ , and the idler is now at very large momentum,  $k_i = 3.6 \mu\text{m}^{-1}$ , where its dispersion is very exciton-like and flat, and thus the idler has a very small group velocity and its own modulations are visible only very close to the defect. For this case, we can appreciate in the idler filtered profile overlapped modulations from all the three state Rayleigh rings (note that because the signal is at negative momentum, its modulations have an opposite direction compared to the ones of pump and idler), while in the signal we can mostly see the signal long wavelength modulations and only very weakly the pump one.

We can compare the different modulation strengths of the three OPO profiles by looking at the color bars plotted next to the profiles. In order to better compare them on the same plot, we show in S. Fig. 6 the one-dimensional OPO filtered emissions along the  $y = 0$  direction for the three cases analysed above. While for the OPO conditions with a signal at  $k_s = 0.0 \mu\text{m}^{-1}$  (middle panel, corresponding to Fig. 2 of the main manuscript), the imprinted modulations from the pump are hardly visible, and can only be appreciated after a Gaussian filter manipulation, both OPO cases with a finite momentum signal result in modulations in the signal with an amplitude of the same order of magnitude of both pump and idler fluids.

In S. Fig. 7 we instead show the real space profiles obtained by setting all off-diagonal couplings in the Bogoliubov matrix  $\mathcal{L}_{\mathbf{k}}$  of Eq. (6) of the main manuscript to zero, resulting in three uncoupled signal (left column), pump (middle column), and idler (right column) fluids. This underlines the importance of the coupling between the three fluids in the three different OPO regimes previously analysed within the linear response approximation. In particular, for the OPO conditions such that the signal has a finite and positive momentum  $\mathbf{k}_s$  (bottom row of S. Fig. 7, which corresponds to the conditions shown in S. Fig. 4), the coupling has little effect and the three fluid respond to the defect in practice in a independent way (each Rayleigh ring influences its own fluid). The OPO condition with a finite and negative momentum  $\mathbf{k}_s$ , which corresponds to the conditions shown in S. Fig. 5, are shown in the top row of S. Fig. 7: Here, we can see that the coupling between the three fluids plays an effect. The modulations of the pump can be appreciated both in the signal profile (though weakly), as well as in the idler profile. In the idler fluid its own modulations can only propagate very close to the defect and thus the only really appreciable modulations are the ones inherited from the pump. Finally, for the experimentally relevant case of an OPO with a signal at zero momentum (middle row of S. Fig. 7, which corresponds to the conditions shown in Fig. 2 of the manuscript), there is also a role played by the coupling, though, as already thoroughly analysed, the modulations in the signal inherited from the pump can only be appreciated after a Gaussian filtering manipula-

tion.

Finally note that, as it also happens for the OPO conditions shown in Fig. 1 of the manuscript, the subsonic to supersonic crossover of the pump-only state<sup>25</sup> happens at pump intensities well above the region of stability of

OPO — the shaded gray regions of S. Figs. 4 and 5 Thus, it is not possible to study a case where the pump is already subsonic and at the same time promotes stimulated scattering.

- 
- \* lorenzo.dominici@gmail.com  
† Corresponding author: francesca.marchetti@uam.es
- <sup>1</sup> A. V. Kavokin, J. J. Baumberg, G. Malpuech, and F. P. Laussy, *Microcavities* (Oxford University Press, Oxford, 2007).
  - <sup>2</sup> C. Ciuti, P. Schwendimann, B. Deveaud, and A. Quattropani, *Phys. Rev. B* **62**, R4825 (2000).
  - <sup>3</sup> C. Ciuti, P. Schwendimann, and A. Quattropani, *Phys. Rev. B* **63**, 041303 (2001).
  - <sup>4</sup> C. Ciuti, P. Schwendimann, and A. Quattropani, *Semicond. Sci. Technol.* **18**, S279 (2003).
  - <sup>5</sup> R. M. Stevenson, V. N. Astratov, M. S. Skolnick, D. M. Whittaker, M. Emam-Ismael, A. I. Tartakovskii, P. G. Savvidis, J. J. Baumberg, and J. S. Roberts, *Phys. Rev. Lett.* **85**, 3680 (2000).
  - <sup>6</sup> P. G. Savvidis, J. J. Baumberg, R. M. Stevenson, M. S. Skolnick, D. M. Whittaker, and J. S. Roberts, *Phys. Rev. Lett.* **84**, 1547 (2000).
  - <sup>7</sup> P. G. Savvidis, J. J. Baumberg, R. M. Stevenson, M. S. Skolnick, D. M. Whittaker, and J. S. Roberts, *Phys. Rev. B* **62**, R13278 (2000).
  - <sup>8</sup> J. J. Baumberg, P. G. Savvidis, R. M. Stevenson, A. I. Tartakovskii, M. S. Skolnick, D. M. Whittaker, and J. S. Roberts, *Phys. Rev. B* **62**, R16247 (2000).
  - <sup>9</sup> M. Saba, C. Ciuti, J. Bloch, V. Thierry-Mieg, R. André, L. S. Dang, S. Kundermann, A. Mura, G. Bongiovanni, J. L. Staehli, and B. Deveaud, *Nature* **414**, 731 (2001).
  - <sup>10</sup> K. Edamatsu, G. Oohata, R. Shimizu, and T. Itoh, *Nature* **431**, 167 (2004).
  - <sup>11</sup> S. Savasta, O. D. Stefano, V. Savona, and W. Langbein, *Phys. Rev. Lett.* **94**, 246401 (2005).
  - <sup>12</sup> L. Lanco, S. Ducci, J.-P. Likforman, X. Marcadet, J. A. W. van Houwelingen, H. Zbinden, G. Leo, and V. Berger, *Phys. Rev. Lett.* **97**, 173901 (2006).
  - <sup>13</sup> M. Abbarchi, V. Ardizzone, T. Lecomte, A. Lemaitre, I. Sagnes, P. Senellart, J. Bloch, P. Roussignol, and J. Tignon, *Phys. Rev. B* **83**, 201310 (2011).
  - <sup>14</sup> V. Ardizzone, M. Abbarchi, A. Lemaitre, I. Sagnes, P. Senellart, J. Bloch, C. Delalande, J. Tignon, and P. Roussignol, *Phys. Rev. B* **86**, 041301 (2012).
  - <sup>15</sup> W. Xie, H. Dong, S. Zhang, L. Sun, W. Zhou, Y. Ling, J. Lu, X. Shen, and Z. Chen, *Phys. Rev. Lett.* **108**, 166401 (2012).
  - <sup>16</sup> T. Lecomte, V. Ardizzone, M. Abbarchi, C. Diederichs, A. Miard, A. Lemaitre, I. Sagnes, P. Senellart, J. Bloch, C. Delalande, J. Tignon, and P. Roussignol, *Phys. Rev. B* **87**, 155302 (2013).
  - <sup>17</sup> I. Carusotto and C. Ciuti, *Rev. Mod. Phys.* **85**, 299 (2013).
  - <sup>18</sup> M. Wouters and I. Carusotto, *Phys. Rev. A* **76**, 043807 (2007).
  - <sup>19</sup> D. Sanvitto, F. Marchetti, M. Szymańska, G. Tosi, M. Baudisch, F. Laussy, D. Krizhanovskii, M. Skolnick, L. Marrucci, A. Lemaitre, J. Bloch, C. Tejedor, and L. V. na, *Nature Physics* **6**, 527 (2010).
  - <sup>20</sup> F. M. Marchetti, M. H. Szymańska, C. Tejedor, and D. M. Whittaker, *Phys. Rev. Lett.* **105**, 063902 (2010).
  - <sup>21</sup> F. M. Marchetti and M. H. Szymańska, “Vortices in polariton opo superfluids,” (Springer-Verlag, 2012) Chap. Exciton Polaritons in Microcavities: New Frontiers.
  - <sup>22</sup> A. J. Leggett, *Rev. Mod. Phys.* **71**, S318 (1999).
  - <sup>23</sup> J. Kasprzak, M. Richard, S. Kundermann, A. Baas, P. Jeanbrun, J. M. J. Keeling, F. M. Marchetti, M. H. Szymańska, R. André, J. L. Staehli, V. Savona, P. B. Littlewood, B. Deveaud, and L. S. Dang, *Nature* **443** (2006).
  - <sup>24</sup> M. Wouters and I. Carusotto, *Phys. Rev. Lett.* **105**, 020602 (2010).
  - <sup>25</sup> A. Amo, J. Lefrère, S. Pigeon, C. Adrados, C. Ciuti, I. Carusotto, R. Houdré, E. Giacobino, and A. Bramati, *Nat. Phys.* **5**, 805 (2009).
  - <sup>26</sup> A. Amo, D. Sanvitto, F. P. Laussy, D. Ballarini, E. del Valle, M. D. Martin, A. Lemaitre, J. Bloch, D. N. Krizhanovskii, M. S. Skolnick, C. Tejedor, and L. V. na, *Nature* **457**, 291 (2009).
  - <sup>27</sup> M. H. Szymanska, F. M. Marchetti, and D. Sanvitto, *Phys. Rev. Lett.* **105**, 236402 (2010).
  - <sup>28</sup> D. M. Whittaker, *Phys. Stat. Sol. (c)* **2**, 733 (2005).
  - <sup>29</sup> A. Amo, S. Pigeon, C. Adrados, R. Houdré, E. Giacobino, C. Ciuti, and A. Bramati, *Phys. Rev. B* **82**, 081301 (2010).
  - <sup>30</sup> J. M. Zajac and W. Langbein, *Phys. Rev. B* **86**, 195401 (2012).
  - <sup>31</sup> M. Wouters and I. Carusotto, *Phys. Rev. B* **75**, 075332 (2007).
  - <sup>32</sup> G. E. Astrakharchik and L. P. Pitaevskii, *Phys. Rev. A* **70**, 013608 (2004).
  - <sup>33</sup> D. M. Whittaker, *Phys. Rev. B* **71**, 115301 (2005).
  - <sup>34</sup> See Supplemental Material at ... for details on the model, used parameters, and numerical procedures.
  - <sup>35</sup> I. Carusotto and G. Rousseaux, “The cerenkov effect revisited: from swimming ducks to zero modes in gravitational analogs,” (2012), arXiv:1202.3494.
  - <sup>36</sup> Even if they do not appear to be relevant here, note that the presence of a non-vanishing imaginary part of the excitation spectrum  $Im\omega_{n,(u,v),\vec{k}} \neq 0$  introduces some complications: Even in the absence of any Rayleigh ring, the drag force can be non-vanishing and the standard Landau criterion may fail identifying a critical velocity<sup>24</sup>.
  - <sup>37</sup> I. Carusotto, S. X. Hu, L. A. Collins, and A. Smerzi, *Phys. Rev. Lett.* **97**, 260403 (2006).
  - <sup>38</sup> I. Carusotto and C. Ciuti, *Phys. Rev. Lett.* **93**, 166401 (2004).
  - <sup>39</sup> D. Ballarini, M. D. Giorgi, E. Cancellieri, R. Houdré, E. Giacobino, R. Cingolani, A. Bramati, G. Gigli, and D. Sanvitto, *Nature Communications* **4**, 1778 (2013).
  - <sup>40</sup> L. Dominici, D. Colas, S. Donati, P. Restrepo Cuartas, J., M. De Giorgi, D. Ballarini, G. Guirales, C. López Carreño, J., A. Bramati, G. Gigli, E. del Valle, P. Laussy, F., and D. Sanvitto, *Phys. Rev. Lett.* **113**, 226401 (2014).